ECLÉTICA QUÍMICA

Eclet. Quim. 51 | e-1583, 2026

Original Articles in Chemistry and Related Areas

https://doi.org/10.26850/1678-4618.eq.v51.2026.e1583

Synthesis and characterization of $Fe_3O_4/SiO_2/C$ nanocomposites and their potential for NH_4^+ ion removal from shrimp farm wastewater

Alif Alfarisyi **Syah**[1], Lukluatus **Syavika**[1], Anugrah Ricky **Wijaya**[1+], Nita **Kusumawati**[2]

Abstract

The synthesized $Fe_3O_4/SiO_2/C$ nanocomposites are adsorbents for NH_4^+ ion removal from shrimp farm effluent. Fe_3O_4 nanomagnets were synthesized via coprecipitation, coated with silica and carbon using 2% NaOH activation, and PEG4000 as a binder. Structural characteristics were investigated through XRD, FT-IR, and VSM. Physico-chemical parameters, including adsorbent amount (0.05–0.3 g), contact time (10–70 min), and initial NH_4Cl concentration (0.1–0.8 mg L^{-1}), were investigated. Maximum NH_4^+ removal efficiency (83.5%) was achieved at 55 min with 0.2 g adsorbent mass, using a solution of 0.4 mg L^{-1} NH_4Cl at pH 7 and 25 °C. Pseudo-second-order kinetic model (R^2 = 0.9998) was satisfied with an adsorption capacity of 0.037 mg g^{-1}. Langmuir isotherm estimated a capacity range of 0.005 to 0.087 mg g^{-1}. The adsorption process occurs exothermically, spontaneously, and is physisorption. Filtrate analysis by UV-Vis with phenate reagents showed notable reduction in NH_4^+ levels post-adsorption (0.077-0.282 mg L^{-1}) with GIS visualization, showcasing effective environmental preservation. These nanocomposites successfully adsorbed NH_4^+ in shrimp pond effluent with potential magnetic recovery.

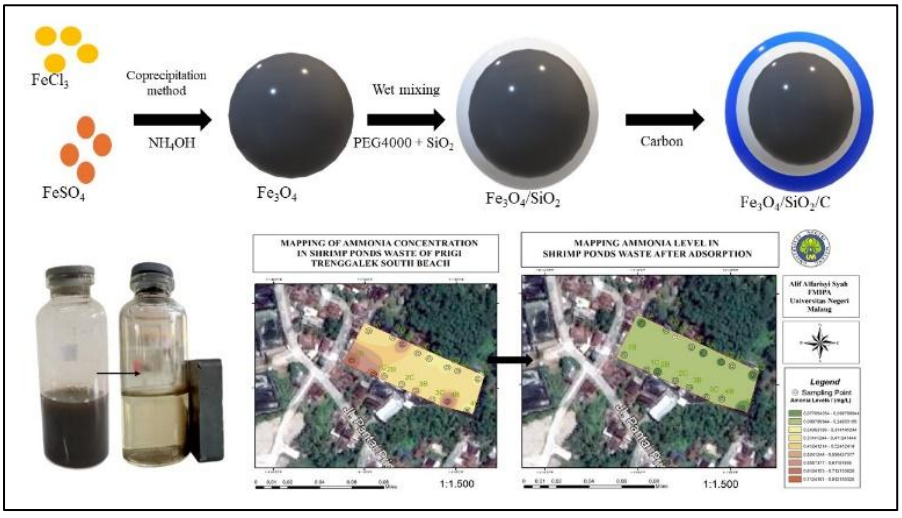

Article History

Received June 21, 2024
Accepted October 04, 2025
Published July 03, 2026

Keywords

1. Magnetic nanocomposites
2. NH_4^+ removal
3. Shrimp waste

Section Editors

Manuel Ignacio Azocar **Guzmán**

Highlights

- $Fe_3O_4/SiO_2/C$ nanocomposites exhibit efficient NH_4^+ adsorption.
- $Fe_3O_4/SiO_2/C$ nanocomposites demonstrate high NH_4^+ adsorption efficacy.
- These nanocomposite effectively reduced NH4+ level from shrimp pond wastewater.
- $Fe_3O_4/SiO_2/C$ nanocomposite mitigates NH_4^+ levels in wastewater.
- $Fe_3O_4/SiO_2/C$ nanocomposites enable NH_4^+ removal from wastewater.

[1]State University of Malang, Faculty of Mathematics and Natural Sciences, Malang, Indonesia. [2]State University of Surabaya, Faculty of Mathematics and Natural Sciences, Surabaya, Indonesia. **+Corresponding author:** Anugrah Ricky Wijaya, **Phone:** +6285755558160, **Email address:** anugrah.ricky.fmipa@um.ac.id

1. Introduction

The coastal region of Prigi Bay has seen significant changes in recent years, particularly with the establishment of shrimp ponds as a means of cultivating these crustaceans. However, this development has raised concerns about the potential environmental impact, especially if organic waste from shrimp farming is not properly managed (Armid *et al.*, 2021; Wijaya *et al.*, 2019a). Prior to the introduction of shrimp ponds, Prigi Bay boasted good water quality, meeting the standards set by the World Health Organization (WHO) (Suci *et al.*, 2020; Wijaya *et al.*, 2019b). Therefore, recent research indicated that the ammonia levels in the wastewater from these shrimp ponds, which are now scattered along the coast, are poised to exceed established thresholds and quality standards, potentially jeopardizing the bay's ecological health (Susetyaningsih *et al.*, 2020). To address this issue, there's a growing need for effective treatment of shrimp pond liquid waste to reduce ammonia concentrations before it's released into the environment (Krishnani *et al.*, 2006). Researchers have carried out exploration to investigate total dissolved and natural sources of metals and organic compound in marine Waters (Wijaya *et al.*, 2022a, 2022b).

The separation of dissolved ammonia, in the form of NH_4^+, can be achieved through various methods, including solvent extraction (both liquid-liquid and liquid-solid colorimetric methods) (Brzezinski, 1987), break point chlorination (Tsitsifli and Kanakoudis, 2018), ion exchange (Sharma and Ahmad, 2018.), and adsorption (Haghighi and Kurd, 2004). Among these methods, adsorption stands out as a highly promising approach due to its remarkable advantages, including high efficiency, exceptional selectivity, cost-effectiveness, and eco-friendliness (Sumantri *et al.*, 2020; Zhang *et al.*, 2016). Here, we focused on the development of adsorbents, which exhibit superior selectivity and efficiency in capturing NH_4^+ on their surfaces.

The magnetic nanomaterial adsorbent is crucial for NH_4^+ ion removal due to their nanoscale size, extensive surface area, and magnetic properties, enabling efficient recycling. However, magnetic nanomaterials tend to agglomerate due to particle attraction, oxidation, and leaching. In this study, we employed the coprecipitation method to synthesize Fe_3O_4 nanomagnetite with SiO_2 and carbon, forming the $Fe_3O_4/SiO_2/C$ nanocomposite (Ardiyanti *et al.*, 2018). SiO_2 serves as a coating to mitigate Fe_3O_4 particle agglomeration (Anbarasu *et al.*, 2019; Feng *et al.*, 2019). Unlike prior research using glucose as an active carbon precursor in Fe_3O_4/C preparation (C. Wang *et al.*, 2019), we utilized mangrove biochar. Mangrove leaf litter with its substantial surface area and negative surface charge enhances cation exchange capacity (CEC) for NH_4^+ adsorption (Ding *et al.*, 2010).

In this research, the effect of carbon on the characteristics of $Fe_3O_4/SiO_2/C$ nanocomposites was also observed. Characterization of carbon, Fe_3O_4 nanoparticles, and $Fe_3O_4/SiO_2/C$ nanocomposites using Fourier Transform Infrared (FT-IR) to identify functional groups, detailed information about the crystallographic structure used X-Ray Diffraction analysis (XRD), measurement of the magnetization used Vibrating-Sample Magnetometry (VSM) methods, Scanning Electron Microscopy and Energy Dispersive X-ray (SEM-EDX) to measure particle diameter, morphology, and elemental content, and Thermogravimetric Analysis - Differential Thermal Analysis (TGA-DTA) to analyze weight changes, thermal stability, and other thermal characteristics. NH_4^+ adsorption was carried out in various variations, including variations in the amount of adsorbent, contact time, temperature, and variations in the concentration of the standard solution, to find the kinetics, thermodynamics, and isotherms of NH_4^+ adsorption by $Fe_3O_4/SiO_2/C$ nanocomposites. The ammonia concentration was determined using the UV-Vis spectrometric method, referring to the phenate method and analysis of mapping levels using ArcGIS software.

2. Experimental details

2.1. Extraction and refining of carbon

The mangrove leaves were thoroughly cleaned and then subjected to oven drying at 60 °C until dryness. Subsequently, the dried mangrove leaves were pulverized and sieved to obtain a 200-mesh-size powder. The resulting mangrove leaf powder was carbonized using a furnace at 400 °C for 2 h. The resulting carbon powder from the dried mangrove leaves was subsequently employed in the next stage (Ding *et al.*, 2010).

The mangrove carbon leaf was chemically activated using 2%w/v NaOH. The carbon was soaked in 2% NaOH for 24 h, then filtered and washed with distilled water until the filtrate solution reached a neutral pH. After the neutralization process, the carbon was oven-dried at 60 °C to eliminate any remaining distilled water (Ding *et al.*, 2010).

2.2. Extraction and refining of silica (SiO_2)

The sand from Prigi Beach was processed by drying it at 60 °C for four days, sieving it to a 100-mesh size, and removing impurities. Subsequently, 120 g of the sand sample were treated with a mixture of 50 mL hot distilled water, 150 mL 37% HCl, and 50 mL 65% HNO_3. The mixture was allowed to settle for 20 h in a fume hood. The reflux method was carried out at approximately 70 °C for 2 h, followed by filtration and neutralization to achieve a pH of 7. The residue was dried for 1 h at 60 °C and then calcined in a furnace at 600 °C for 4 h.

Furthermore, the calcined sand sample was subjected to three cycles of evaporation by adding 30 mL hot distilled water and 30 mL concentrated HCl, followed by heating on a hot plate within a fume hood. An additional treatment was conducted with 30 mL of concentrated HCl at 60 °C for 35 min. The residue from this process was neutralized with distilled water, resulting in 40 grams of white silica powder.

2.3. Synthesis Fe_3O_4 nanoparticles

The synthesis of Fe_3O_4 nanoparticles followed the same procedure as the prior study, encompassing the subsequent steps: A mixture of 75 mL of 0.19 mol/L $FeSO_4{\cdot}7H_2O$ solution and 75 mL of 0.25 mol/L $FeCl_3{\cdot}6H_2O$ solution was combined in a 250 mL beaker. The mixture was then heated to a temperature of 90 °C, and 10 mL of 25% NH_4OH was added. This solution was stirred for 30 min using a magnetic stirrer. The resulting black precipitate was filtered using distilled water until it reached a neutral pH of 7. The precipitate was subsequently dried in an oven at a temperature of 50-60 °C for a duration of 5 h. To achieve homogeneity, the solids obtained were ground using a mortar and pestle (Rianna *et al.*, 2022).

2.4. Synthesis $Fe_3O_4/SiO_2/C$ nanocomposites

The synthesis of $Fe_3O_4/SiO_2/C$ composite was carried out by adding polyethylene glycol (PEG) through the wet mixing method (**Fig. 1**). The first step was to start by melting 0.7 g of PEG 4000 by stirring and heating it at 60 °C, 0.7 g SiO_2 powder was then added while still stirring until mixed. 0.7 g Fe_3O_4 powder and 0.7g of carbon powder were added and stirred until mixed and formed

https://doi.org/10.26850/1678-4618.eq.v51.2026.e1583

precipitate. The precipitate was then dried in an oven at 35 °C to form $Fe_3O_4/SiO_2/C$ powder (Feng *et al.*, 2019).

Figure 1. The application of $Fe_3O_4/SiO_2/C$ nanomagnetite by an external magnet.
Source: Elaborated by the authors.

2.5. Characterization of Fe_3O_4 nanoparticles and $Fe_3O_4/SiO_2/C$ composites

The first characterization of Fe_3O_4 and $Fe_3O_4/SiO_2/C$ nanoparticles was carried out using an infrared spectrometer (FTIR, Shimadzu IR Prestige 21) to determine the functional groups of the compounds. Furthermore, determining the crystallinity was characterized by XRD (PANalytical X'Pert Pro), while VSM (DXV-100~550 Series) was employed to determine the magnetic moment. SEM-EDX (Merk FEI, Type: Inspect-S50) were employed in conjunction with ImageJ to measure particle diameter, morphology, and elemental content, and TGA-DTA (Merk Linseiss, Type: STA PT 1600) to analyze weight changes, thermal stability, and other thermal characteristics.

2.6. The NH_4^+ adsorption experiment

The NH_4^+ adsorption experiment was conducted using a batch technique. Initially, different amounts of $Fe_3O_4/SiO_2/C$ nanocomposite, such as 0.01, 0.05, 0.1, 0.15, 0.2, and 0.3 g, were entered into separate Erlenmeyer flasks. Subsequently, 10-50 mL of a 0.4 mg L^{-1} NH_4^+solution was added to each flask. The Erlenmeyer was shaken at 150 rpm for one hour. The purpose of the experiment was to determine the optimum amount of mass adsorbent. The variation of contact time between adsorbent and adsorbate from 10 to 70 min was carried out to determine the optimum contact time, and the variation of NH_4Cl standard solution from 0.1 to 0.8 mg L^{-1} was used to determine the optimum concentration. The optimum temperature was set at 300.15–333 K. The solutions were filtered using Whatman 42 filter paper to separate the nanocomposite from the solution. The resulting filtrate was analyzed to determine the NH_4^+ concentration using phenate reagent and UV-Vis spectroscopy at a wavelength of 640 nm. The result was the concentration at equilibrium NH_4^+, and to calculate the amount of NH_4^+ adsorbed on the adsorbent $Fe_3O_4/SiO_2/C$ under various conditions. The **Eq. 1** was used:

$$q_e = \frac{(Co - Ce) \cdot V}{m} \quad (1)$$

The qe (mg g^{-1}) shows the adsorption capacity. C_o and C_e (mg L^{-1}) indicate the NH_4^+ concentration before and after the adsorption process, respectively. m (g) and V (L) are the adsorbent mass and the volume of the solution, respectively. The percentage of adsorption NH_4^+ is calculated using the **Eq. 2**.

$$\text{Adsorption } \% = \frac{Co - Ce}{Co} \times 100 \quad (2)$$

3. Result and discussion

3.1. Characterization of Fe_3O_4 nanoparticles, SiO_2, carbon, and $Fe_3O_4/SiO_2/C$ nanocomposites

The FTIR serves as a valuable tool for analyzing the absorption patterns of atomic functional groups in materials. We conducted FTIR tests on Fe_3O_4, SiO_2, carbon and the $Fe_3O_4/SiO_2/C$ nanocomposite, as shown in **Fig. 2**. The analysis focuses on the correlation between wavenumbers and transmittance. We also verify and match functional groups based on prior research.

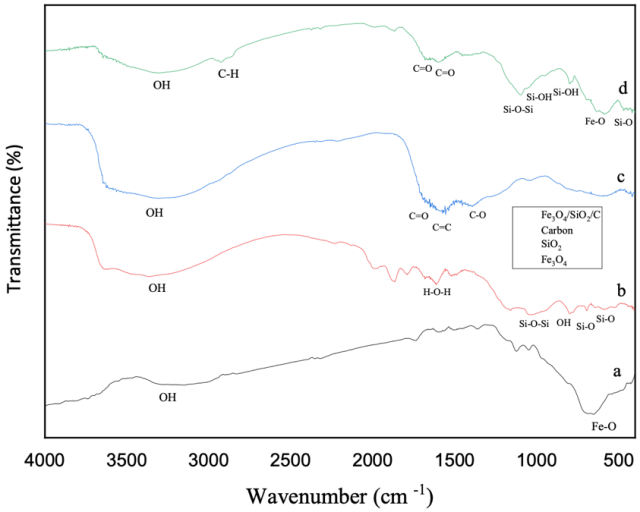

Figure 2. The infrared spectra of **(a)** Fe_3O_4, **(b)** SiO_2, **(c)** Carbon, **(d)** $Fe_3O_4/SiO_2/C$ nanocomposites synthesized with PEG as binder.
Source: Elaborated by the authors.

Our investigation involves the examination of functional groups within the Carbon, SiO_2, and ferrimagnetic Fe_3O_4 core-shell samples, within the infrared absorption range of 500–4000 cm^{-1}. Notable findings include Si-O bond rocking vibrations at 468 cm^{-1}, O-H (silanol) bond vibrations within the range of 800-870 cm^{-1}, which is a characteristic of the SiO_2 molecule, and O-H bond vibrations related to water molecules within the range of 1050–1115 cm^{-1}. The presence of Fe_3O_4 in $Fe_3O_4/SiO_2/C$ is indicated by Fe-O-Fe group vibrations between 572–587 cm^{-1}. Symmetrical stretching vibrations of Si-O-Si and Si-O bonds occur at wavenumbers of 793, 1092-1098 cm^{-1}, and 954-964 cm^{-1}. Additionally, the C=O group appears at absorptions of 1693.56 and 1697.41 cm^{-1}, which is a typical group in active carbon (Pires *et al.*, 2015), while the C-O bond vibrations at 1342 and 1635 cm^{-1} were caused by the influence of the PEG media binder. The functional group for the H-C-H bond was at 1351 and 1637 cm^{-1} (Munasir *et al.*, 2017). Referring to the C_2H bond vibration, a CH (water molecule) may also occur at 2919 and 3313 cm^{-1} functional groups like the H-C-H bond are detected at 1351 and 1637 cm^{-1}. Vibrations associated with CH (water molecule) and O-H functional groups occur at 2919 and 3313 cm^{-1}.

Our initial characterization serves the purpose of determining the crystalline structure and phases present in the Fe_3O_4 and carbon within the $Fe_3O_4/SiO_2/C$ nanocomposite samples. We analyze the XRD pattern of both Fe_3O_4 nanoparticles

https://doi.org/10.26850/1678-4618.eq.v51.2026.e1583

and $Fe_3O_4/SiO_2/C$ nanocomposites, as shown in **Fig. 3**. This analysis involves a comparison of the diffraction peaks of Fe_3O_4 with the reference data obtained from the Crystallography Open Database (COD) under ID number 1011052. Cubic Fe_3O_4 adopts a face-centered structure. The positions of the diffraction peaks at 2θ: 30.18, 35.55, 43.20, 53.57, 57.15, and 62.78° correspond to the (111), (220), (311), (400), (422), (511), and (440) planes of Fe_3O_4, respectively. Meanwhile, the broad diffraction pattern observed within the 2θ range of approximately 11-23° signifies the presence of a non-crystalline (amorphous) carbon phase. Further diffraction patterns for Fe_3O_4 and carbon coincide with PEG diffraction peaks at 2θ values around 19 and 23°, indicative of the PEG's diffraction pattern (Dindar *et al.*, 2010). These diffraction patterns provide confirmation of the successful formation of the $Fe_3O_4/SiO_2/C$ composites.

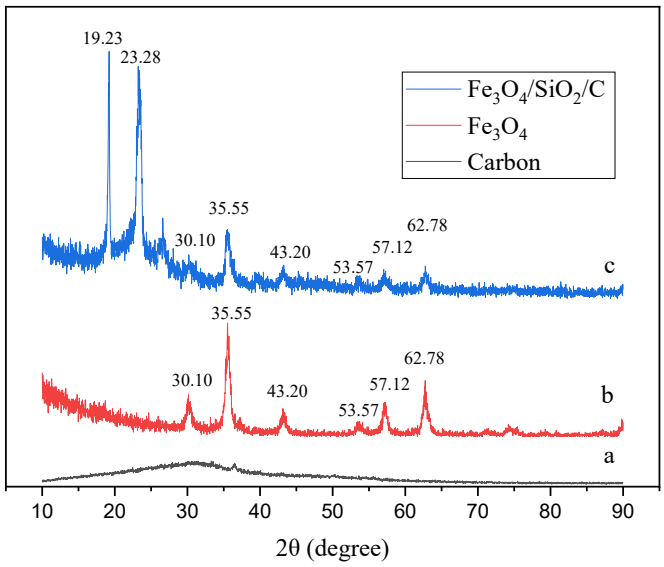

Figure 3. XRD Patterns of **(a)** Fe_3O_4, **(b)** Carbon, **(c)** $Fe_3O_4/SiO_2/C$ nanocomposites synthesized with PEG as binder.
Source: Elaborated by the authors.

The magnetic properties of Fe_3O_4, and $Fe_3O_4/SiO_2/C$ were analyzed (**Fig. 4**), showing superparamagnetic behavior with no hysteresis loops, indicating their potential for magnetic separation and reuse in adsorption-desorption processes. The saturation magnetization (Ms) values were measured at 56.13 and 16.68 emu g^{-1} for the magnetic Fe_3O_4 mixed with Fe_2O_3, and $Fe_3O_4/SiO_2/C$, respectively. The SiO_2 and carbon coating led to a decrease in saturation magnetization, but the material could still be easily separated from the reaction medium using an external magnet. This suggests that the nanocomposite remains suitable for magnetic separation and reuse as an adsorbent, as even an Ms value of around 8 emu g^{-1} was reported (Han *et al.*, 2018), which shows a sufficient magnetic response for this purpose. The magnetic separation of $Fe_3O_4/SiO_2/C$ could be achieved within 40 sec (**Fig. 4**) by placing a magnet near the vessel containing the suspension. The SiO_2 and Carbon coating's main effect was reflected in the temperature dependence of the high field, with deviations from the Bloch law at low temperatures, associated with the occurrence of surface spin disordered effects (Larumbe *et al.*, 2012).

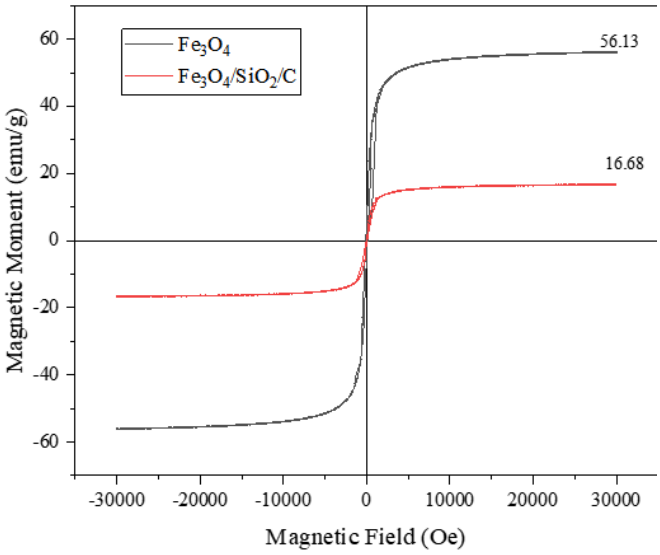

Figure 4. Magnetic curves of Fe_3O_4 and $Fe_3O_4/SiO_2/C$ nanocomposites synthesized with PEG as binder.
Source: Elaborated by the authors.

The measurement results of the particle size distribution of Fe_3O_4 nanoparticles (**Fig. 5a**) indicate that the particles exhibit mesoporous sizes ranging from 2 to 50 nm, with an average diameter of 26.4 nm, classifying them as nanomaterials (1–100 nm). Some particles agglomerate to form larger aggregates due to van der Walls forces and magnetic core attraction (Ma'rufah *et al.*, 2019; Rianna *et al.*, 2022) with a maximum size of 146.2 nm. Other studies have shown that agglomerated particles can reach sizes of 4-6 µm depending on the synthesis method (Rianna *et al.*, 2022). Furthermore, Transmission Electron Microscopy (TEM) is recommended for future studies to provide more accurate particle size analysis. The EDX analysis (**Fig. 5b**) reveals that the composition of Fe_3O_4 nanoparticles consists of 66.2% iron (Fe) and 33.8% oxygen (O) without any impurities (Rianna *et al.*, 2022; Tatinting *et al.*, 2021).

The results of SEM analysis indicate that $Fe_3O_4/SiO_2/C$ nanoparticles (**Fig. 6a**) exhibit homogeneous morphology with a consistent pore distribution on the surface, making them ideal for ammonium ion (NH_4^+) adsorption. The adsorption of NH_4^+ depends on the surface area and pore size of the adsorbent, with nanoparticles featuring smaller pore sizes facilitating stronger interactions with NH_4^+ ions (Zheng *et al.*, 2019). Measurements conducted using ImageJ software on SEM images at a magnification of 20,000x (**Fig. 6b**) reveal an average particle diameter of 82.6 nm, with the smallest particle measuring 72.7 nm and the largest measuring 98.9 nm. This size is larger than that of the Fe_3O_4 particles, indicating aggregation during synthesis due to the addition of PEG, SiO_2 (Antarnusa *et al.*, 2022; Feng *et al.*, 2019). This study successfully synthesized nanocomposites within the nanomaterial category (1-100 nm).

The SEM-EDX analysis of the $Fe_3O_4/SiO_2/C$ nanocomposite (**Fig. 7**) reveals four main elements: carbon (C) at 65.8%, oxygen (O) at 27.3%, aluminum (Al) at 0.2%, silicon (Si) at 3.4%, and iron (Fe) at 3.2%. The elevated levels of carbon and oxygen are attributed to the biochar carbon in the composite. The lower iron percentage is due to the SEM-EDX technique, which primarily scans the sample surface. This data reflects the surface composition of the nanocomposite, indicating successful synthesis of $Fe_3O_4/SiO_2/C$ with minimal impurities, specifically aluminum from silica alumina.

https://doi.org/10.26850/1678-4618.eq.v51.2026.e1583

The thermal stability of the $Fe_3O_4/SiO_2/C$ (Fig. 8) nanocomposite was analyzed using TGA and DTA over a temperature range of 19-1000 °C. The TGA curve indicates a mass loss of 5.92% between 19-190 °C, attributed to the removal of adsorbed water molecules and hydroxyl groups. A second mass loss of 16.01% occurs between 190-451 °C due to the decomposition of hydroxyl functional groups and the degradation of the carbon structure. The third mass loss of 3.01% between 450-874.4 °C is associated with the condensation of silanol groups into siloxane and the decomposition of organic residues (Fattahi and Dekamin, 2023). The nanocomposite remains stable at temperatures between 450-921 °C, with a total mass loss of only 3%. The DTA curve displays both endothermic and exothermic signals. Endothermic peaks at 306.7°C and 387.9°C are related to the decomposition of carboxylate groups and the release of CO_2. The exothermic peaks indicate the thermal degradation of residual lignin, hemicellulose, and cellulose between 268-400 °C (Vu *et al.*, 2018). An endothermic signal at 501-802 °C signifies the phase transition from magnetite (Fe_3O_4) to hematite (Fe_2O_3) (Mazo-Zuluaga *et al.*, 2003; Mahdavi *et al.*, 2013). Hematite stabilizes at 507 °C, but its stability decreases due to the deoxidation process (Zhao *et al.*, 2006).

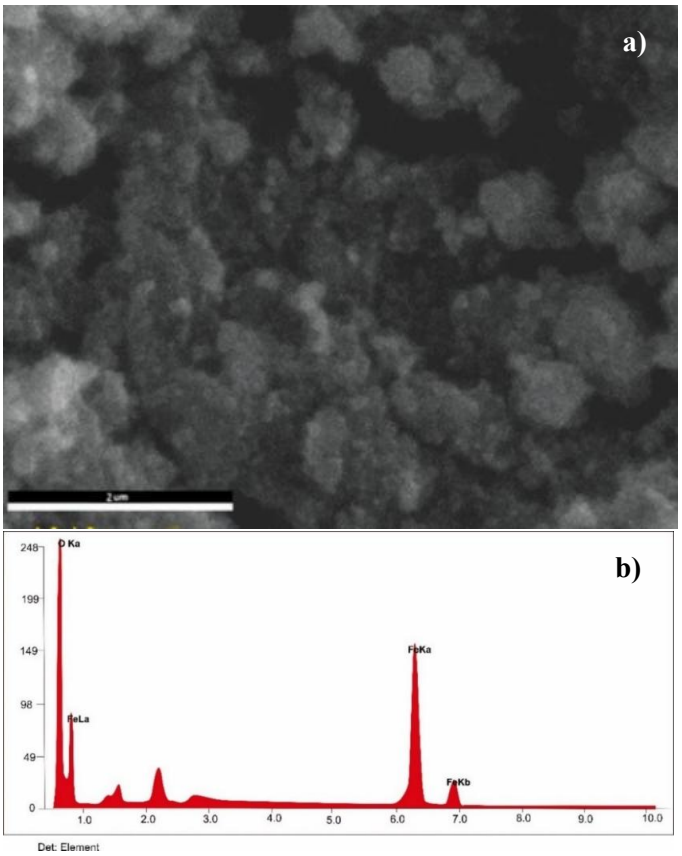

Figure 5. SEM **(a)** results and EDX **(b)** spectrum of nanoparticles Fe_3O_4.
Source: Elaborated by the authors.

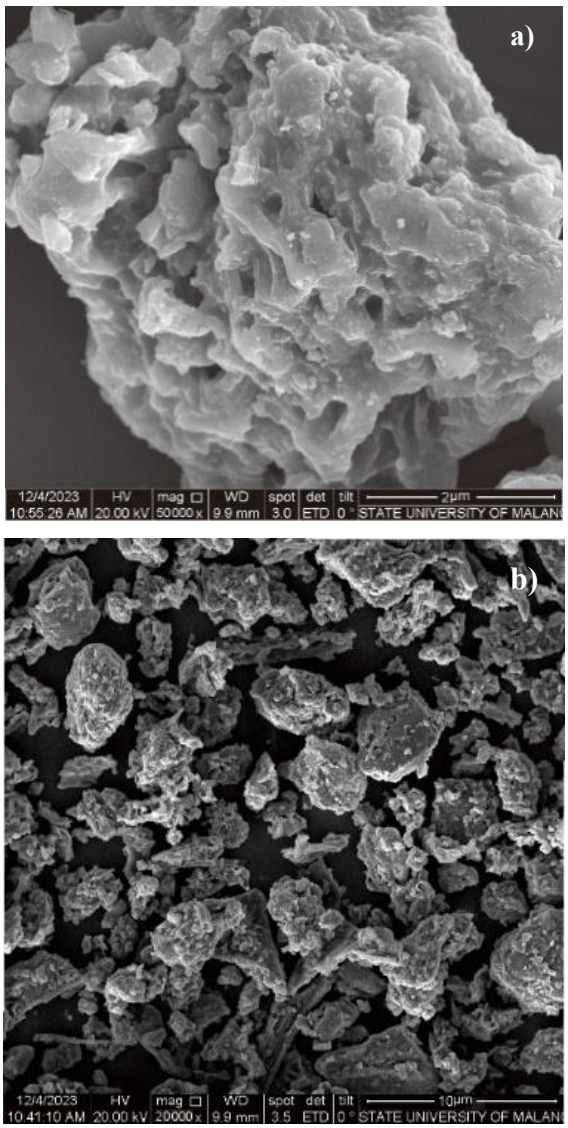

Figure 6. SEM photos of nanocomposites $Fe_3O_4/SiO_2/C$ enlargement **(a)** 50000x, and **(b)** 20000x.
Source: Elaborated by the authors.

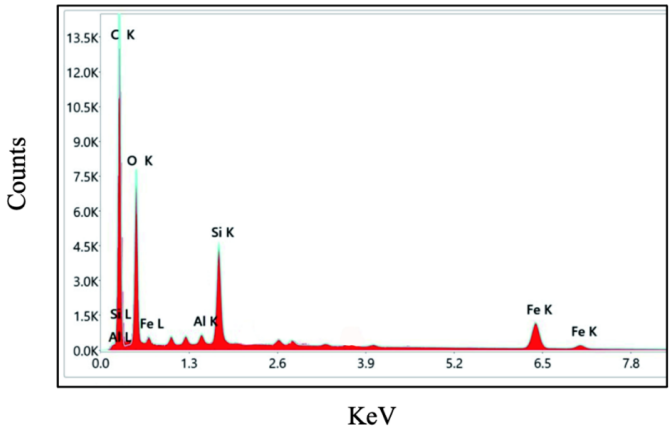

Figure 7. EDX spectrum of nanoparticles $Fe_3O_4/SiO_2/C$.
Source: Elaborated by the authors.

https://doi.org/10.26850/1678-4618.eq.v51.2026.e1583

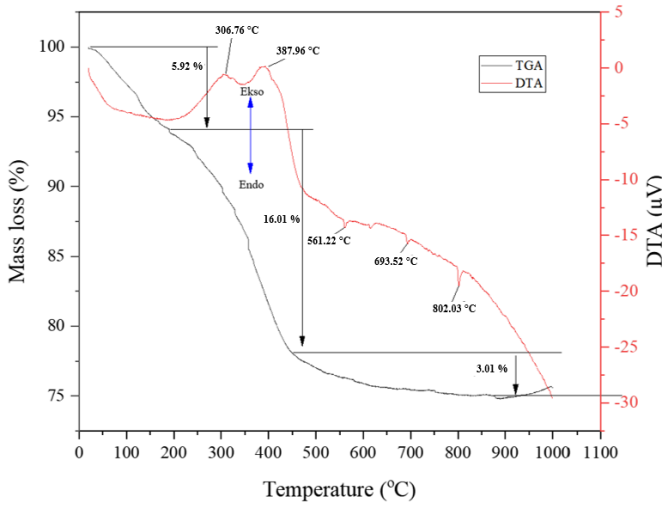

Figure 8. TGA/DTA analysis curve of $Fe_3O_4/SiO_2/C$ nanocomposite.
Source: Elaborated by the authors.

3.2. Influence the amount of adsorbent and contact time

The efficiency of NH_4^+ adsorption is in direct correlation with the amount of adsorbent applied, and this relationship is illustrated in **Fig. 9a**. A remarkable 83.4% NH_4^+ adsorption efficiency was achieved when 0.2 grams of adsorbent were employed. The escalation in adsorbent mass release, in an increased number of active sites, significantly enhances the adsorption capacity of NH_4^+ by $Fe_3O_4/SiO_2/C$ nanocomposites. Consequently, the optimal adsorbent mass selected for our investigation stands at 0.2 g.

The influence of contact time on NH_4^+ adsorption by $Fe_3O_4/SiO_2/C$ nanocomposites is investigated, as shown in **Fig. 9b**. It is evident that adsorption levels increase with extended contact time. Maximum adsorption occurred after 55 min, followed by a decrease in adsorption at 70 min of contact time. The optimal equilibrium adsorption capacity for NH_4^+ was 0.023 mg g^{-1} at 55 min, decreasing to 0.020 mg g^{-1} at 70 min. This phenomenon is attributed to the adsorbate molecules not entirely binding to the active sites of the adsorbent due to saturation, resulting in partial desorption and a subsequent decrease after the optimum condition. This suggests that as contact time increases, the available surface area decreases, affecting the adsorbent's ability to adsorb NH_4^+ molecules. Concurrently, the rate of NH_4^+ molecule desorption increases until it reaches equilibrium. This indicates that the adsorbent has reached its optimal contact time (Galamini *et al.*, 2020; Sohaimi *et al.*, 2021; Tabak *et al.*, 2010).

3.3. Adsorption kinetics of NH_4^+

The adsorption kinetics of NH_4^+ were examined, involving the assessment of NH_4^+ adsorption by $Fe_3O_4/SiO_2/C$ nanocomposites over a range of contact times spanning from 10 to 70 min. To analyze the NH_4^+ adsorption data, we employed both the pseudo-first order and pseudo-second order kinetic models. These models are characterized by linear **Eq. 3** and **Eq. 4**, as expressed below:

Pseudo-first-order equation:

$$\log(q_{e-}\ q_t\ ) = \log q_{e-} \frac{k_1 t}{2.303} \quad (3)$$

Pseudo-second-order equation:

$$\frac{t}{q_t} = \frac{1}{k_2 q_e^2} + \frac{1}{q_e} \quad (4)$$

where, q_t (mg g^{-1}) and q_e (mg g^{-1}) serve as indicators of the quantity of NH_4^+ absorbed at a given time and at equilibrium, respectively. In the context of the pseudo-first order and pseudo-second order kinetic equations, k_1 (min^{-1}) and k_2 (g/mg min) represent the rate constants. The determination of these rate constants, k_1 and k_2, involves analyzing the gradient of the natural logarithm of (q_e - q_t) against time (t) and the intercept of the graph of w against t, as presented in **Fig. 10a** (Aurich *et al.*, 2017). Analysis data of the initial concentration, concentration at some time, and concentration at equilibrium are processed to find out the appropriate kinetics model. The results of the experiments are carried out at 25 °C (298 K), initial NH_4^+ concentration of 0.4 mg L^{-1}, volume of solution 25 mL, and weight of $Fe_3O_4/SiO_2/C$ nanocomposites 0.2 g are presented in **Table 1**.

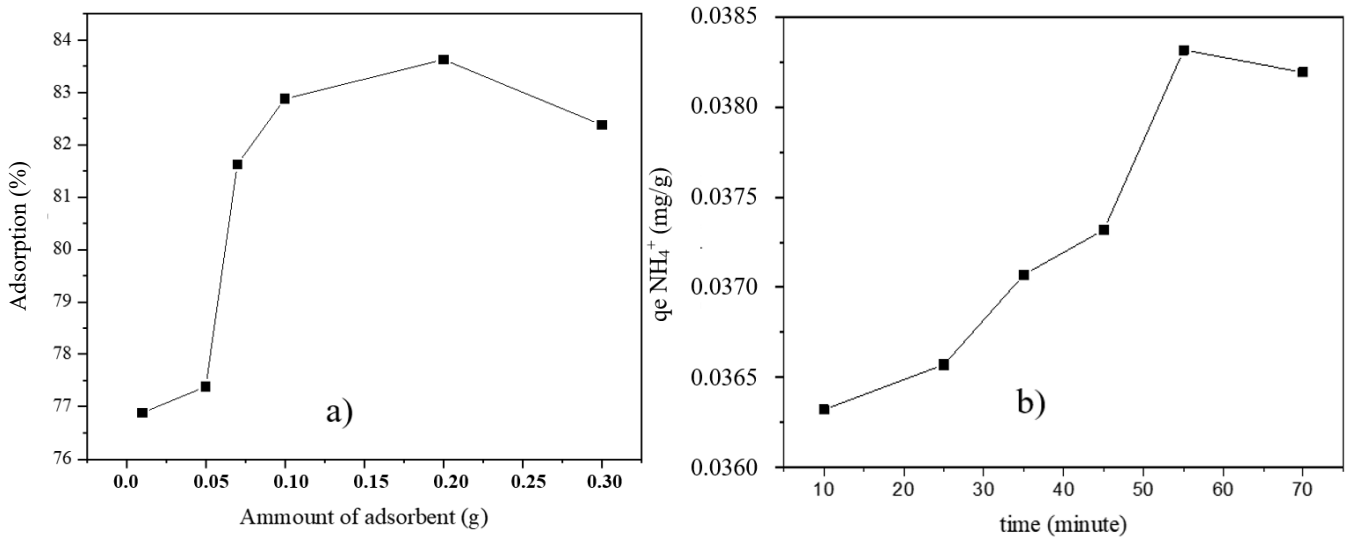

Figure 9. Influence of the sum of adsorbent **(a)**, contact time **(b)**.
Source: Elaborated by the authors.

https://doi.org/10.26850/1678-4618.eq.v51.2026.e1583

Table 1. Experimental results at 25 °C (298 K), contact time 10-70 min.

Time (min)	C_t (mg L^{-1})	q_t (mg g^{-1})	log(q_e - q_t)	t/q_t (min g.mg^{-1})
0	0.400	0	−0.398	0
10	0.109	0.0363	−2.700	275.326
25	0.107	0.0366	−2.758	683.618
35	0.103	0.0371	−2.904	944.175
45	0.101	0.0373	−3.001	1205.819
55	0.093	0.0383	-	1565.863
70	0.126	0.0382	−3.904	1832.810

Source: Elaborated by the authors.

In this study, the adsorption kinetics followed a pseudo-second order model (**Fig. 10b**). The linear regression coefficient (R^2) indicates that the pseudo-second-order kinetics model provides a more suitable explanation for the NH_4^+ adsorption process by $Fe_3O_4/SiO_2/C$ nanocomposites (**Table 2**). This assumes that the extended contact between nanocomposites and NH_4^+ ions elevates the time-to-capacity ratio, causing the valence forces' impact on shared electron usage between the adsorbent surface and organic molecules, influencing the adsorption rate.

The pseudo-second order model is a better fit for the experimental data of NH_4^+ adsorption by $Fe_3O_4/SiO_2/C$ compared to the first-order pseudo model. This is due to the q_e value (0.037 mg g^{-1}) calculated using the pseudo-second order model, which was almost close to the experimental q_e value (0.038 mg g^{-1}), and the correlation coefficient (R^2) of the pseudo-second order model was higher than that of the pseudo-first order model. The higher R^2 value indicates a better fit of the model to the experimental data. The pseudo-second order model assumes chemisorption or strong surface complexation, which is more likely to occur in the case of NH_4^+ adsorption by $Fe_3O_4/SiO_2/C$. Therefore, the results suggest that the dominant mechanism controlling the rate of NH_4^+ adsorption is strong surface complexation or chemical adsorption.

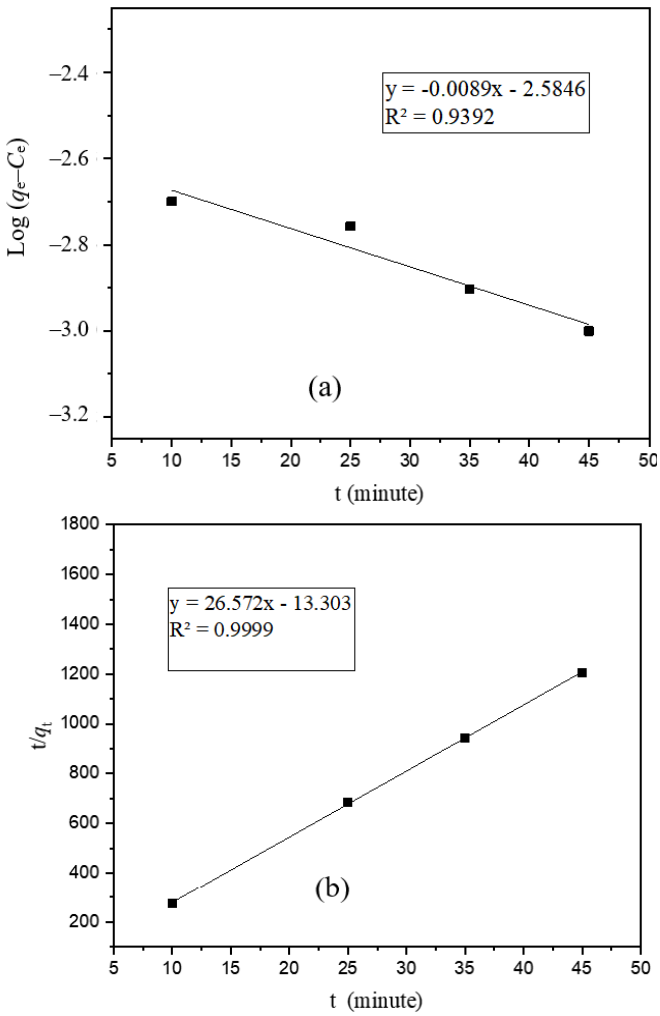

Figure 10. Adsorption kinetics curves **(a)** pseudo-first order; **(b)** pseudo-second order.
Source: Elaborated by the authors.

Table 2. Kinetic parameters of uranium adsorption by $Fe_3O_4/SiO_2/C$ based on pseudo-first order and pseudo-second order.

Ion Ammonium	Pseudo-first order				Pseudo-second order		
	$q_{e,exp}$	$q_{e,cal}$	k_1 (min^{-1})	R^2	q_e (Calorie)	k_2 (g mg^{-1} min^{-1})	R^2
NH_4^+	0.038	0.0026	0.0205	0.932	0.037	53.075	0.999

Source: Elaborated by the authors.

3.4. Isotherm adsorption of NH_4^+

The adsorption capacity is estimated by using adsorption equilibrium models in this research. Two equilibrium models are employed: the Langmuir and the Freundlich adsorption isotherms. The Langmuir isotherm suggests that the adsorbent surface contains multiple active sites where molecules bind (monolayer), while the Freundlich isotherm assumes a heterogeneous surface. The assessment of NH_4^+ adsorption by $Fe_3O_4/SiO_2/C$ nanocomposites covers a concentration range of the standard solution from 0.1 to 0.8 mg L^{-1}. To evaluate the NH_4^+ adsorption data, linear equations representing these models are utilized, as shown by **Eq. 5** and **Eq. 6**.

Freundlich model equation:

$$\log_{q_e} = \log K_{f+} \frac{1}{n} log C_e \quad (5)$$

Langmuir model equation:

$$\frac{C_e}{q_e} = \frac{1}{K_L\, q_m} + \frac{C_e}{q_m} \quad (6)$$

In the equations, q_m (mg g^{-1}) represents the maximum monolayer adsorption capacity, while q_e (mg g^{-1}) is the equilibrium amount of NH_4^+ adsorbed per unit mass of the sorbent. *Ce* (mg L^{-1}) stands for the equilibrium concentration of ammonium ions in the aqueous solution, and *Co* (mg L^{-1}) is the initial ammonium ion concentration. K_L (L/mg) is the Langmuir constant related to adsorption energy, and K_f (mg g^{-1}), along with $1/n$ are associated with the sorbent's adsorption capacity and the intensity of the adsorption process (heterogeneity parameter), respectively (Sharifnia *et al.*, 2016). The experimental parameters are in **Table 3**. **Figure 11** depicts the adsorption isotherm of ammonium ions using the nanocomposite adsorbent over the initial concentration range of 0.1-0.8 mg L^{-1}.

Table 3. Experimental results at 25 °C (298 K), initial NH_4^+ concentration of 0.1-0.8 mg L^{-1}.

C_o	C_e (mg L^{-1})	C_o-C_e	q_e (mg g^{-1})	$1/q_e$ (g mg^{-1})	$1/C_e$ (L mg^{-1})	log C_e	log q_e
0.1	0.057	0.043	0.005	184.275	17.672	-1.247	-2.265
0.2	0.080	0.120	0.015	66.414	12.572	-1.099	-1.822
0.4	0.088	0.312	0.039	25.633	11.376	-1.026	-1.409
0.6	0.099	0.501	0.063	15.965	10.109	-1.005	-1.203
0.8	0.103	0.697	0.087	11.475	9.723	-0.988	-1.060

Source: Elaborated by the authors.

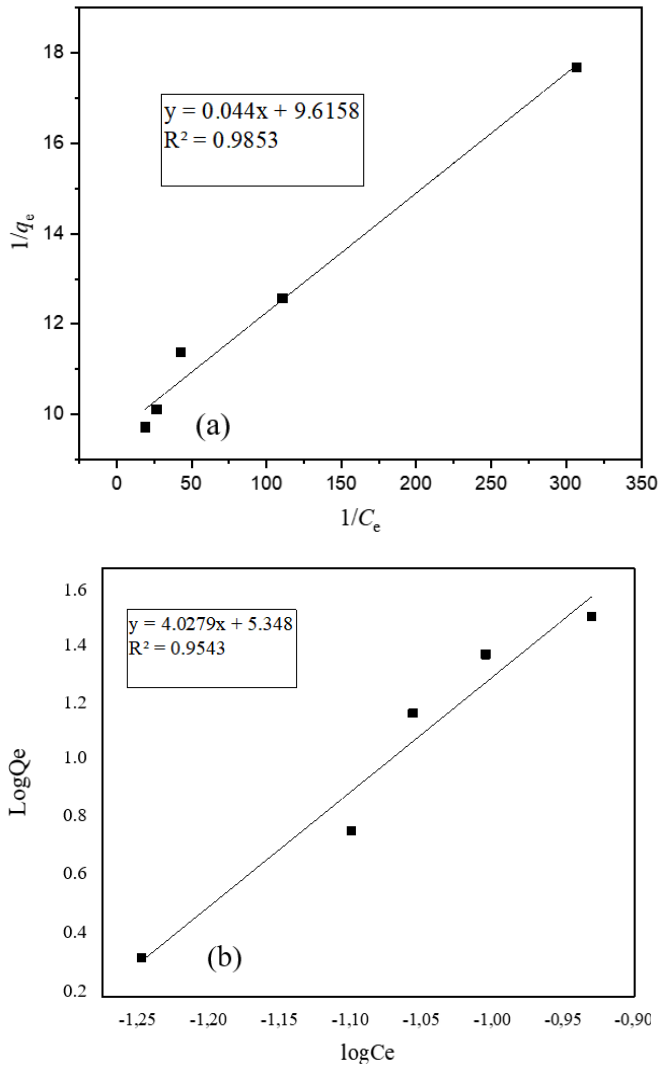

Figure 11. Isotherm adsorption curves for **(a)** Langmuir; **(b)** Freundlich.
Source: Elaborated by the authors.

The adsorption isotherm follows the Langmuir isotherm type (**Fig. 11a**). The linear regression coefficient (R^2) for the Langmuir isotherm is higher than that of the Freundlich isotherm (**Fig. 11b**), with values of 0.9853 and 0.9543, respectively. These results indicate that the NH_4^+ adsorption by the nanocomposite can be better explained by the Langmuir isotherm. In the Langmuir isotherm, the adsorption mechanism involves a chemisorption process with the occurrence of chemical bonds between the adsorbent and adsorbate. The Langmuir model states that the existing valence forces can attract adsorbed molecules to the surface of the adsorbent (Syafiuddin *et al.*, 2018; Utomo *et al.*, 2012).

The explanation provided earlier states that the pseudo-second-order kinetics model is used to describe the adsorption rate on the surface, based on the assumption of strong surface complexation, which is consistent with the Langmuir adsorption isotherm by stating that the adsorption rate occurs in parallel with the remaining solute concentration. In the context of the adsorbent and adsorbate reaction, this model indicates that the adsorption reaction occurs through a chemical mechanism involving the compatibility between the donor and acceptor molecules on the adsorbate surface (Syafiuddin *et al.*, 2018; Utomo *et al.*, 2012). This model is characterized by a higher correlation coefficient (R^2) and a better fit to the experimental data compared to the pseudo-first-order model. On the other hand, the Langmuir adsorption is used to describe monolayer adsorption on a surface containing a limited number of identical sites. The relationship between the two lies in the fact that the equation of the Langmuir isotherm model leads to the equation of the second-order kinetic model, which explains monolayer adsorption on a surface containing a limited number of identical sites. The compatibility between the adsorbate and adsorbent molecules occurs through strong binding between the donor and acceptor atoms on the adsorbate surface (Sharifnia *et al.*, 2016; Utomo *et al.*, 2012).

3.5. Thermodynamic adsorption of NH_4^+

The mechanism by which temperature affects NH_4^+ adsorption can be confirmed using thermodynamic parameters of adsorption (ΔG, ΔH, and ΔS). These parameters can be calculated based on thermodynamic laws using the following equations: where the equilibrium constant (K_L) is related to the amount of ammonium ions (C_a) adsorbed onto the adsorbent from the solution at equilibrium (mg/L) (**Eq. 7**), while C_S is the equilibrium concentration of ammonium ions in the aqueous solution (mg/L). ΔH (enthalpy change) and ΔS (entropy change) are derived from the slope and intercept of the van't Hoff plot of $ln\ K_C$ versus 1/T (**Eq. 8**). The results of these calculations are presented in **Table 4**. Gibbs free energy (**Eq. 9**) indicates the spontaneity of the adsorption process, where more negative values suggest a more favorable adsorption process.

$$K_L = \frac{C_a}{C_s} \quad (7)$$

van't Hoff equations:

$$ln\ k_L = \frac{\Delta S^O}{R} - \frac{\Delta H^O}{RT} \quad (8)$$

$$\Delta G^O = \Delta H^O - T\Delta S^O \quad (9)$$

More negative ΔG values reflect an easier process. Generally, the free energy change for physisorption ranges from −20 to 0 kJ/mol, while chemisorption ranges from −80 to −400 kJ/mol (Uğurlu *et al.*, 2008; Uurlu and Karaolu, 2011). In this study, ΔG for the adsorption of NH_4^+ ions by the $Fe_3O_4/SiO_2/C$ nanocomposite was observed to be −3.834 kJ/mol at 300.15 K and −1.607 kJ/mol at 333 K. Additionally, the calculated ΔH for the $Fe_3O_4/SiO_2/C$ nanocomposite is −24.09 kJ/mol. The negative ΔH value indicates that the adsorption process of NH_4^+ ions onto the $Fe_3O_4/SiO_2/C$ nanocomposite is exothermic (releasing heat). The low ΔH value reflects weak interactions between NH_4^+ ions and the

negatively charged sites on the $Fe_3O_4/SiO_2/C$ surface. The negative entropy change (ΔS) for ammonium adsorption on $Fe_3O_4/SiO_2/C$ (−67.47 J/mol K) concludes that this adsorption process is spontaneous at low temperature ranges (Boopathy *et al.*, 2013).

Table 4. Thermodynamic parameters of NH_4^+ adsorption of $Fe_3O_4/SiO_2/C$ nanocomposites.

Ion	ΔG^o (kJ/mol)					ΔH^o (kJ/mol)	ΔS^o (J/mol·K)
NH_4^+	300.15	303.15	313 K	323 K	333 K	−24.09	−67.47
	−3.834	−3.631	−2.957	−2.282	−1.607		

Source: Elaborated by the authors.

3.6. FTIR Spectra analysis before and after the NH_4^+ adsorption process by $Fe_3O_4/SiO_2/C$ nanocomposites

The analysis of NH_4^+ adsorption by the $Fe_3O_4/SiO_2/C$ nanocomposite (**Fig. 12**) using FTIR spectroscopy reveals significant changes in the wave numbers of several functional groups after adsorption. The shift of the OH group from 3313.5 to 3394.3 cm^{-1} indicates a chemical interaction between NH_4^+ ions and hydroxyl groups. Minor changes were also observed in the C=O bonds (from 1670.2 and 1600.1 to 1672.3 and 1636.6 cm^{-1}) and C-O bonds (from 1417.3 to 1394.5 cm^{-1}), suggesting the involvement of carboxyl and hydroxyl groups in bonding with NH_4^+.The increase in peaks within the OH region indicates the diffusion of water vapor from the air into the nanocomposite during the batch application method, enhancing the sharpening of O-H bonds in the FTIR spectrum (R. yu Wang *et al.*, 2019; Rahman *et al.*, 2017). The minor changes in the vibrational modes of carboxylate and hydroxyl groups after adsorption imply that the quantity of $Fe_3O_4/SiO_2/C$ nanocomposite exceeds the concentration of the adsorbed NH_4^+ ions (R. yu Wang *et al.*, 2019; Rahman *et al.*, 2017; Shooto, 2020). According to Ainane *et al.* (2014), changes in vibrational intensity with minimal positional shifts confirm that the adsorption process is of the inclusion type, where molecules or ions are trapped within the porous structure of the adsorbent (Ainane *et al.*, 2014). This observation is also applicable to the $Fe_3O_4/SiO_2/C$ nanocomposite in the adsorption of NH_4^+ ions.

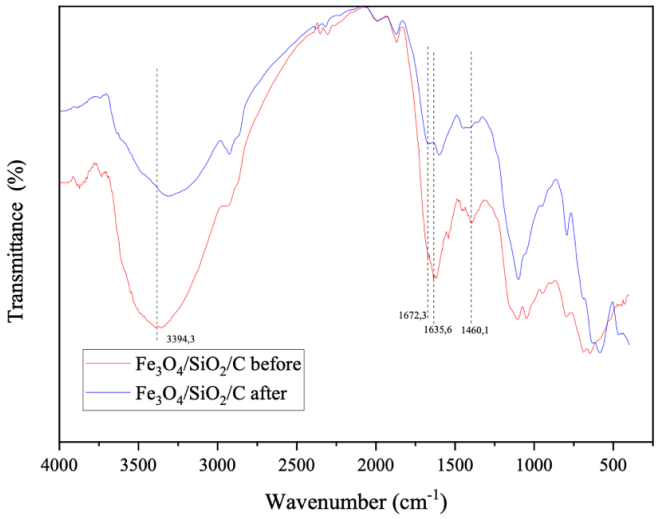

Figure 12. FTIR spectrum **(a)** before and **(b)** after adsorption.
Source: Elaborated by the authors.

3.7. Mapping adsorption of NH_4^+ in shrimp farm wastewater

Figure 13 illustrates the location of shrimp farm wastewater and **Table 5** reveals that the investigation carried out at 16 pond locations indicates that the wastewater contains ammonia levels surpassing the established quality standard. The table illustrates that the data on ammonia levels in wastewater exceeds the >0.2 mg L^{-1} threshold set by the US-EPA.

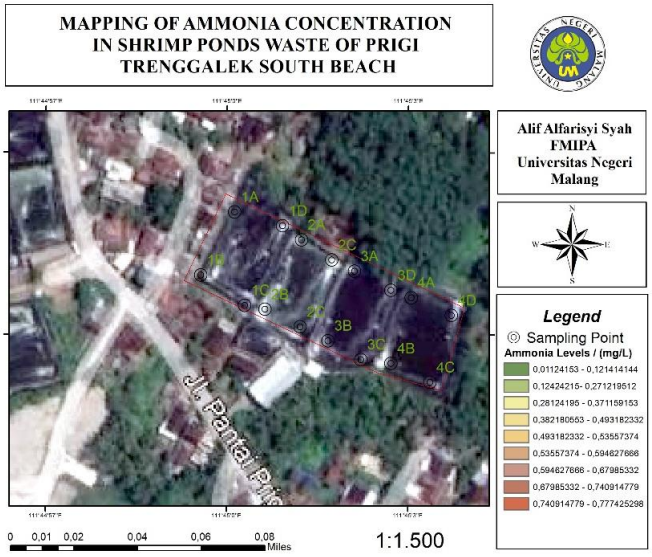

Figure 13. Sampling location: shrimp farm wastewater using ArcGIS.
Source: Elaborated by the authors.

According to the data presented, it is evident that the ammonia content in the wastewater is within the range of 0.321–0.771 mg L^{-1}. Elevated levels of total ammonia in the water can be attributed to various factors, including shrimp excretion, stocking density, aquatic organisms, and environmental conditions. Shrimp feed, rich in protein at 40%, contributes to the release of toxic ammonia compounds as the feed decomposes and settles in the sediments. Therefore, this study employs $Fe_3O_4/SiO_2/C$ nanocomposite adsorbents to mitigate ammonia concentrations in shrimp pond wastewater.

Table 5. Ammonia Level in the water of the shrimp farm of Prigi Bay.

Location	ABS	NH_4^+ levels (mg L^{-1})
1A	0.397	0.388
1B	0.745	0.735
1C	0.781	0.771
1D	0.419	0.410
2A	0.651	0.642
2B	0.383	0.374
2C	0.369	0.360
2D	0.447	0.438
3A	0.341	0.332
3B	0.519	0.510
3C	0.373	0.364
3D	0.335	0.326
4A	0.461	0.452
4B	0.706	0.697
4C	0.329	0.320
4D	0.364	0.355

Source: Elaborated by the authors.

The concentration of ammonia for marine aquatic organisms is less than 0.3 mg L^{-1}, while the US-EPA standard requires a concentration below 0.1 mg L^{-1}. Elevated ammonia levels in aquatic environments can harm the quality of dissolved oxygen and have an impact on aquatic organisms. Most of the ammonia originates from commercial shrimp feed used in ponds, with most of it being discharged into the environment. This discharge can pose a threat to aquatic ecosystems and lead to eutrophication. Consequently, an efficient method is required to reduce ammonia levels in shrimp pond wastewater. **Figure 14** illustrates the NH_4^+ adsorption process with $Fe_3O_4/SiO_2/C$.

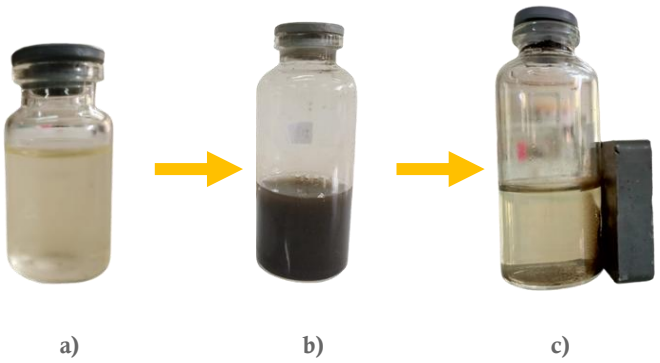

Figure 14. Examples of the absorption of NH_4^+ by $Fe_3O_4/SiO_2/C$ **(a)** wastewater shrimp farm, **(b)** after the addition of adsorbent, and **(c)** absorption of NH_4^+ by $Fe_3O_4/SiO_2/C$ adsorbent.
Source: Elaborated by the authors.

As shown in **Fig. 14a-c**, a bottle containing NH_4^+ solution was incorporated with $Fe_3O_4/SiO_2/C$ powder, and it appeared black. The solution was then shaken and allowed to settle (1–2 min). The sample wastewater shrimp farm changed color to nano-spare black. The next step is to place an external magnet, as shown in **Fig. 14c**. The pure water and NH_4^+ absorbed by $Fe_3O_4/SiO_2/C$ particles were separated in the external magnetic field.

Figure 15 shows the adsorption mapping of shrimp farm wastewater by $Fe_3O_4/SiO_2/C$ adsorbent before **(a)**, and after adsorption **(b)**. Samples were subjected to adsorption using nanocomposite $Fe_3O_4/SiO_2/C$ with optimized amount and duration, followed by UV-Vis phenate analysis.

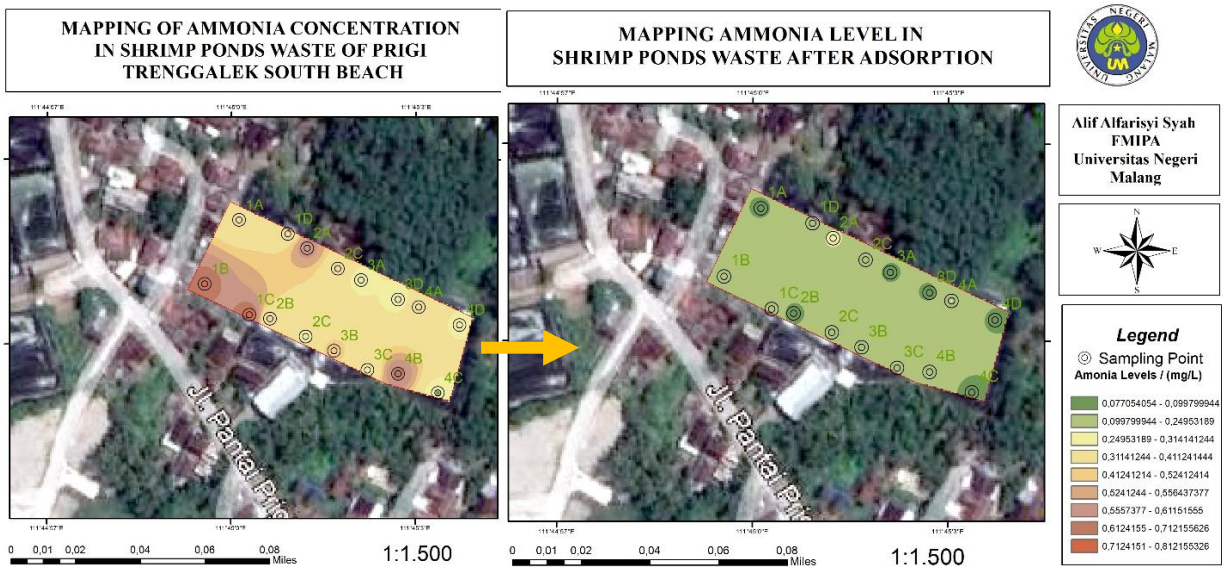

Figure 15. Adsorption mapping of shrimp farm wastewater by $Fe_3O_4/SiO_2/C$ adsorbent before **(a)**, and after adsorption **(b)**.
Source: Elaborated by the authors.

As shown in **Fig. 15** the subsequent ArcGIS mapping illustrated a significant reduction in shrimp pond wastewater levels, with concentrations decreasing from the initial range of 0.321-0.771 mg L^{-1} (**Fig. 15a**) to a range of 0.077-0.282 mg L^{-1} (**Fig. 15b**). This substantial reduction, ranging from 42.7% to 82.1%, underscores the effectiveness of the method in environmental preservation. It particularly addresses the issue of mitigating the discharge of ammonia-rich wastewater from shrimp ponds, emphasizing the potential for broader environmental benefits.

7. Conclusions

$Fe_3O_4/SiO_2/C$ nanocomposites were successfully synthesized, and carbon was used to efficiently extract from mangrove leaf biochar. SiO_2 were also successfully extracted from silica sand. The synthesis of $Fe_3O_4/SiO_2/C$ nanocomposites was effectively carried out using PEG as a binder. Fe_3O_4 nanoparticles with a SiO_2/C layer provided numerous functional group components, such as Fe-O, Si-O-Si, Si-OH, C-H, OH^-, which were advantageous for supporting the adsorption process. The optimal

conditions for NH_4^+ adsorption by the nanocomposites were determined as an adsorbent mass of 0.2 g and a contact time of 55 min. Pseudo-second-order models, Langmuir isotherm types can be used to explain the adsorption of NH_4^+ by $Fe_3O_4/SiO_2/C$ nanocomposites, and the adsorption process occurs exothermically, spontaneously, and is physisorption. Application of $Fe_3O_4/SiO_2/C$ nanocomposites in reducing NH_4^+ levels in shrimp pond wastewater resulted in a substantial reduction, ranging from 42.7% to 82.1%, showing the effectiveness of this method in environmental conservation.

Authors' contribution

Conceptualization: Alif Alfarisyi Syah; Anugrah Ricky Wijaya; **Data curation:** Anugrah Ricky Wijaya; Alif Alfarisyi Syah; **Formal Analysis:** Nita Kusumawati; Alif Alfarisyi Syah; Anugrah Ricky Wijaya; **Funding:** Anugrah Ricky Wijaya; **Investigation:** Alif Alfarisyi Syah; Anugrah Ricky Wijaya; **Methodology:** Alif Alfarisyi Syah; Anugrah Ricky Wijaya; Nita Kusumawati; **Project administration:** Lukluatus Syavika; **Resources:** Alif Alfarisyi Syah; Anugrah Ricky Wijaya; **Software:** Alif Alfarisyi Syah; **Supervision:** Anugrah Ricky Wijaya; Nita Kusumawati; **Validation:** Anugrah Ricky Wijaya; Nita Kusumawati; **Visualization:** Alif Alfarisyi Syah; Lukluatus Syavika; **Writing–original draft:** Alif Alfarisyi Syah; Anugrah Ricky Wijaya; **Writing –review & editing:** Anugrah Ricky Wijaya; Lukluatus Syavika; Alif Alfarisyi Syah.

Conflict of interest

The authors declare that there is no conflict of interest.

Data availability statement

All data generated or analyzed during this study are included in this published article.

Artificial Intelligence usage statement

The authors declare that they used Grammarly for spelling and grammar checks during manuscript preparation and ChatGPT-4 for improving the English language and clarity of the abstract. No generative AI was used to create scientific content. All text was reviewed by the authors.

Funding

This research was supported by the PNBP Universitas Negeri Malang through the Thesis Master Research Grant 2023, No. 5.4.1/UN32/KP/2023.

Acknowledgments

We sincerely thank all members of the Wijaya project and PNBP Universitas Negeri Malang for funding through the Master Thesis Research Grant 2023, No. 5.4.1/UN32/KP/2023. We also thank the anonymous editors and reviewers for their valuable comments and suggestions that improved this manuscript.

References

Ainane, T.; Khammour, F.; Talbi, M.; Elkouali, M. A novel bio-adsorbent of mint waste for dyes remediation in aqueous environments: Study and modeling of isotherms for removal of methylene blue. *Orient. J. Chem*. **2014**, *30*, 1183–1189. https://doi.org/10.13005/ojc/300332

Anbarasu, M.; Anandan, E.; Chinnasamy, V.; Gopinath, K. B. Synthesis and characterization of Fe_3O_4/SiO_2 composite with in-situ method: TEOS as SiO2 NPs precursor. *Journal of Physics: Conference Series.* **2019**, *1171* (1), 6–11. https://doi.org/10.1088/1742-6596/1171/1/012050

Antarnusa, G.; Jayanti, P. D.; Denny, Y. R.; Suherman, A. Utilization of co-precipitation method on synthesis of Fe_3O_4/PEG with different concentrations of PEG for biosensor applications. *Materialia*, **2022**, *25*, 101525. https://doi.org/10.1016/j.mtla.2022.101525

Ardiyanti, H.; Puspitarum, D; Maryana, O. F.; Pujakesuma, W. A. Synthesis and Bonding Analysis of Magnetite Composite Based on Sugarcane Bagasse. ICOSITER 2018 Proceeding, *J. Sci. Appl. Technol*. **2018**, 197–200.

Armid, A.; Shinjo, R.; Takwir, A.; Ruslan, R.; Wijaya, A. R. Spatial distribution and pollution assessment of trace elements Pb, Cu, Ni, Fe and as in the surficial water of Staring Bay, Indonesia. *J. Braz. Chem. Soc*. **2021**, *32*, 299–310. https://doi.org/10.21577/0103-5053.20200180

Aurich, A.; Hofmann, J.; Oltrogge, R.; Wecks, M.; Gläser, R.; Blömer, L.; Mauersberger, S.; Müller, R. A.; Sicker, D.; Giannis, A. Pseudo-second order model for sorption processes Y.S. *Org. Process Res. Dev*. **2017**, *21*, 866–870. https://doi.org/10.1021/acs.oprd.7b00090

Boopathy, R.; Karthikeyan, S.; Mandal, A. B.; Sekaran, G. Adsorption of ammonium ion by coconut shell-activated carbon from aqueous solution: kinetic, isotherm, and thermodynamic studies. *Environmental Science and Pollution Research*. **2013**, *20* (1), 533–542. https://doi.org/10.1007/s11356-012-0911-3

Brzezinski, M. A. Colorimetric determination of nanomolar concentrations of ammonium in seawater using Reagents **1987,** *20*, 277–288. https://doi.org/10.1016/0304-4203(87)90078-8

Dindar, M. H.; Fathi, S. A. M.; Yaftian, M. R.; Noushiranzadeh, N. Solid phase extraction of copper(II) ions using C18-silica disks modified by oxime ligands. *J. Hazard. Mater*. **2010**, *179*, 289–294. https://doi.org/10.1016/j.jhazmat.2010.02.092

Ding, Y.; Liu, Y. X.; Wu, W. X.; Shi, D. Z.; Yang, M.; Zhong, Z. K. Evaluation of biochar effects on nitrogen retention and leaching in multi-layered soil columns. *Water. Air. Soil Pollut*. **2010**, *213*, 47–55. https://doi.org/10.1007/s11270-010-0366-4

Fattahi, B.; Dekamin, M. G. Fe_3O_4/SiO_2 decorated trimesic acid-melamine nanocomposite: a reusable supramolecular organocatalyst for efficient multicomponent synthesis of imidazole derivatives. *Sci. Rep*. **2023**, *13*, 1–13. https://doi.org/10.1038/s41598-023-27408-7

Feng, S.; Wang, R.; Bai, Y.; Yang, S.; Ma, Q.; Yilihamu, A.; Yang, S.-T.; Luo, J. $Fe_3O_4/SiO_2/C$ nanocomposites for the fenton-like disinfection of Escherichia coli in water Fe_3O_4/ SiO_2/C nanocomposites for the fenton-like disinfection of Escherichia coli in water. *Mater. Res. Express.* **2019**, *6* (5) 055032. https://doi.org/10.1088/2053-1591/ab0585

Galamini, G.; Ferretti, G.; Medoro, V.; Tescaro, N.; Faccini, B.; Coltorti, M. Isotherms, kinetics, and thermodynamics of NH_4^+ adsorption in raw liquid manure by using natural chabazite zeolite-rich tuff. *Water Switz*. **2020**, *12*, 1–16. https://doi.org/10.3390/w12102944

Haghighi, B.; Kurd, S. F. Sequential flow injection analysis of ammonium and nitrate using gas phase molecular absorption spectrometry. *Talanta*. **2004**, *64*, 688–694. https://doi.org/10.1016/j.talanta.2004.03.037

Han, J., Rong, J.; Wang, Y., Liu, Q.; Tang, X.; Li, C.; Ni, L. Immobilization of cellulase on thermo-sensitive; agnetic microspheres: improved stability and reproducibility. *Bioprocess Biosyst. Eng*. **2018**, *41*, 1051–1060. https://doi.org/10.1007/s00449-018-1934-z

Krishnani, K. K.; Parimala, V.; Gupta, B. P.; Azad, I. S.; Meng, X.; Abraham, M. Bagasse-Assisted Bioremediation of Ammonia from Shrimp Farm Wastewater. *Water Environ. Res*. **2006**, *78*, 938–950. https://doi.org/10.2175/106143005x72911

Larumbe, S.; Gómez-Polo, C.; Pérez-Landazábal, J. I.; Pastor, J. M. Effect of a SiO_2 coating on the magnetic properties of Fe_3O_4 nanoparticles. *J. Phys. Condens. Matter Inst. Phys. J.* **2012**, *24*, 266007. https://doi.org/10.1088/0953-8984/24/26/266007

Mahdavi, M.; Ahmad, M. B.; Haron, M. J.; Namvar, F.; Nadi, B.; Rahman, M. A. Z.; Amin, J. Synthesis, surface modification and characterisation of bio;ompatible magnetic iron oxide nanoparticles for

biomedical applications. *Molecules*. **2013**, *18*, 7533–7548. https://doi.org/10.3390/molecules18077533

Ma'rufah, H.; Rohmaniah, S.; Aripin, M.; Sutanto, H. Sintesis Material Nano Fe_3O_4 Dari Karat Besi Yang Berpotensi Diaplikasikan Sebagai Solar Absorber Pada Quantum Dot Sensitized Solar Cell (QDSSC). *Berk. Fis*. **2019**, *22*, 117–122.

Mazo-Zuluaga, J.; Barrero, C. A.; Díaz-Terán, J.; Jerez, A. Thermally Induced Magnetite-Haematite Transformation. *Hyperfine Interact*. **2003**, *148*, 153–161. https://doi.org/10.1023/B:HYPE.0000003776.84005.89

Munasir, M.; Dewanto, A. S.; Yulianingsih, A.; Saadah, I. K. F.; Supardi, Z. A. I.; Mufid, A.; Taufiq, A. Composites of Fe3O4/SiO2 from Natural Material Synthesized by Co-Precipitation Method. IOP Conf. Ser. Mater. Sci. Eng. 2017, 202. https://doi.org/10.1088/1757-899X/202/1/012057

Pires, N. R.; Santos, C. M. W.; Sousa, R. R.; De Paula, R. C. M.; Cunha, P. L. R.; Feitosa, J. P. A. Novel and fast microwave-assisted synthesis of carbon quantum dots from raw cashew gum. J. *Braz. Chem. Soc*. **2015**, *26*, 1274–1282. https://doi.org/10.5935/0103-5053.20150094

Rahman, M. W.; Ali, M. Y.; Saha, I.; Al Raihan, M.; Moniruzzaman, M.; Alam, M. J.; Deb, A.; Khan, M. M. R. Date palm fiber as a potential low-cost adsorbent to uptake chromium (VI) from industrial wastewater. *Desalination Water Treat*. **2017**, *88*, 169–178. https://doi.org/10.5004/dwt.2017.21402

Rianna, M.; Hamid, M.; Handayani, F.; Sebayang, A. M. S.; Rangkuti, W. R.; Situmorang, M.; Sembiring, T.; Setiadi, E. A.; Tetuko, A. P.; Sebayang, P. Study and characterization of Fe3O4 synthesized from natural iron sand in Sumatera Utara. *J. Aceh Phys. Soc.* **2022**, *11*, 45–48. https://doi.org/10.24815/jacps.v11i2.23492

Sharifnia, S., Khadivi, M.A., Shojaeimehr, T., Shavisi, Y. Characterization, isotherm and kinetic studies for ammonium ion adsorption by light expanded clay aggregate (LECA). *J. Saudi Chem. Soc*. **2016**, *20*, S342–S351. https://doi.org/10.1016/j.jscs.2012.12.003

Sharma, S.; Ahmad, W. The classification, characterization, and application of ion exchange resins: A general survey. International Conference on New Horizons in Green Chemistry & Technology (ICGCT) 2018.

Shooto, N. D. Removal of toxic hexavalent chromium (Cr(VI)) and divalent lead (Pb(II)) ions from aqueous solution by modified rhizomes of Acorus calamus. *Surf. Interfaces*. **2020**, *20*, 100624. https://doi.org/10.1016/j.surfin.2020.100624

Sohaimi, K. S. A.; Iberahim, N. I.; Ghani, A. A.; Zamrud, Z.; Heng, C. W. Ammonium adsorption - Desorption using rice husk biochar. *IOP Conf. Ser. Earth Environ. Sci*. **2021**, *765*, 012061. https://doi.org/10.1088/1755-1315/765/1/012061

Suci, C. W.; Wijaya, A. R.; Santoso, A.; Kusumaningrum, I. K. Fe leaching in the sludge sediment of the prigi beach with tessier-microwave method. *AIP Conf. Proc*. **2020**, *2231*, 040025. https://doi.org/10.1063/5.0002589

Sumantri, I.; Buchori, L.; Mukti, F. A. W.; Ramadhani, F.; Anggoro, D. D. Study of the rate of adsorption of toxic gases in shrimp ponds using Sukabumi natural zeolite. *AIP Conf. Proc*. **2020**, *2197*, 120005. https://doi.org/10.1063/1.5140962

Susetyaningsih, R.; Suntoro, S.; Gunawan, T.; Sri Budiastuti, M. T. Impact of shrimp pond waste on water quality (case study of trisik lagoon in yogyakarta). *AIP Conf. Proc*. **2020**, *2296*, 020050. https://doi.org/10.1063/5.0030551

Syafiuddin, A.; Salmiati, S.; Jonbi, J.; Fulazzaky, M. A. Application of the kinetic and isotherm models for better understanding of the behaviors of silver nanoparticles adsorption onto different adsorbents. *J. Environ. Manage*. **2018**, *218*, 59–70. https://doi.org/10.1016/j.jenvman.2018.03.066

Tabak, A.; Baltas, N.; Afsin, B.; Emirik, M.; Caglar, B.; Eren, E. Adsorption of Reactive Red 120 from aqueous solutions by cetylpyridinium-bentonite. *J. Chem. Technol. Biotechnol*. **2010**, *85*, 1199–1207. https://doi.org/10.1002/jctb.2416

Tatinting, G. D.; Aritonang, H. F.; Wuntu, A. D. Sintesis Nanopartikel Fe_3O_4–polietilen glikol (PEG) 6000 Dari Pasir Besi Pantai Hais Sebagai Adsorben Logam Kadmium (Cd). *Chem. Prog*. **2021**, *14* (2), 131-137. https://doi.org/10.35799/cp.14.2.2021.37192

Tsitsifli, S.; Kanakoudis, V. Disinfection Impacts to Drinking Water Safety—A Review. *Proceedings*. **2018**, *2* (11), 603. https://doi.org/10.3390/proceedings2110603

Ramírez-Chavarría, R. G.; Santamaria-Padilla, L.; Vera-Martínez, D. Modeling and analysis of ion exchange for ammonium removal from groundwater. *Mem. Congr. Nac. Control Automático*. **2024**, *7*, 91–96. https://doi.org/10.58571/CNCA.AMCA.2024.016

Rianna, M.; Hamid, M.; Handayani, F.; Sebayang, A. M.S.; Rangkuti, W. R.; Situmorang, M.; Sembiring, T.; Setiadi, E. A.; Tetuko, A.P.; Sebayang, P. Study and characterization of Fe3O4 synthesized from naturaliron sand in Sumatera Utara. J. Aceh Phys. Soc. 2022, 11, 45–48. https://doi.org/10.24815/jacps.v11i2.23492

Uğurlu, M.; Gürses, A.; Yalçın, M.; Doğar, C. The removal of lignin and phenol from paper mill effluents by electrocoagulation. *Journal of Environmental Management*. **2008**, *87* (3), 420–428. https://doi.org/10.1016/j.jenvman.2007.01.007

Uğurlu, M.; Karaoğlu, M. H. Adsorption of methylene blue dye by sepiolite clay: Determination of equilibrium and kinetic parameters. *Microporous and Mesoporous Materials*. **2011**, *139* (1-3), 173–178. https://doi.org/10.1016/j.micromeso.2010.10.031

Utomo, S. B.; Jumina, J. Siswanta, D.; Mustofa, M. Kinetics and equilibrium model of Pb(II) and Cd(II) adsorption onto tetrakis-thiomethyl-C-4-methoxyphenylcalix[4]resorcinarene. *Indones. J. Chem*. **2012**, *12,* 49–56. https://doi.org/10.22146/ijc.21371

Vu, M. T.; Chao, H. P.; Van Trinh, T.; Le, T. T.; Lin, C. C.; Tran, H. N. Removal of ammonium from groundwater using NaOH-treated activated carbon derived from corncob wastes: Batch and column experiments. *J. Clean. Prod.* **2018**, *180*, 560–570. https://doi.org/10.1016/j.jclepro.2018.01.104

Wang, C.; Zhong, H.; Wu, W.; Pan, C.; Wei, X.; Zhou, G.; Yang, F. Fe_3O_4 @ C Core − Shell Carbon Hybrid Materials as Magnetically Separable Adsorbents for the Removal of Dibenzothiophene in Fuels. *ACS Omega*. **2019**, *4*, 1652−1661. https://doi.org/10.1021/acsomega.8b03157

Wang, R. yu; Zhang, W.; Zhang, L. ying; Hua, T.; Tang, G.; Peng, X. qian; Hao, M. hui; Zuo, Q. ting. Adsorption characteristics of Cu(II) and Zn(II) by nano-alumina material synthesized by the sol-gel method in batch mode. *Environ. Sci. Pollut. Res*. **2019**, *26*, 1595–1605. https://doi.org/10.1007/s11356-018-3453-5

Wijaya, A. R.; Khoerunnisa, F.; Armid, A.; Lusiana, R. A. The best-modified BCR and Tessier with microwave-assisted methods for leaching of Cu/Zn and their δ65Cu/δ66Zn for tracing sources in marine sediment fraction. *Environ. Technol. Innov*. **2022a**, *28*, 102663. https://doi.org/10.1016/j.eti.2022.102663

Wijaya, A. R.; Kusumaningrum, I. K.; Hakim, L.; Francová, A.; Chrastný, V.; Vítková, M.; Vaňková, Z.; Komárek, M. Road-side dust from central Jakarta, Indonesia: Assessment of metal(loid) content, mineralogy, and bioaccessibility. *Environ. Technol. Innov*. **2022b**, *28*, 102934. https://doi.org/10.1016/j.eti.2022.102934

Wijaya, A. R.; Oktaviana, I.; Wonorahardjo, S.; Utomo, Y.; Muntholib, M.; Daupor, H.; Hossain, M. S.; Sanjaya, E. H. Optimization of BCR Microwave from Fe Assessment in Sediment Material in the Gulf of Prigi. *IOP Conf. Ser. Mater. Sci. Eng*. **2019a**, *515*, 012091. https://doi.org/10.1088/1757-899X/515/1/012091

Wijaya, A. R.; Semedi, B.; Lusiana, R. A.; Armid, A.; Muntholib, M. Metal contents and Pb isotopes in the surface seawater of the Gulf of Prigi, Indonesia: Detection of anthropogenic and natural sources. *J. Braz. Chem. Soc*. **2019b**, 30, 915–929. https://doi.org/10.21577/0103-5053.20180228

Zhang, H.; Liang, X.; Yang, C.; Niu, C.; Wang, J.; Su, X. Nano γ-Fe2O3/bentonite magnetic composites: Synthesis, characterization and application as adsorbents. *J. Alloys Compd*. **2016**, *688*, 1019–1027. https://doi.org/10.1016/j.jallcom.2016.07.036

Zhao, S. Y.; Don, K. L.; Chang, W. K.; Hyun, G. C.; Young, H. K.; Young, S. K. Synthesis of magnetic nanoparticles of Fe3O4 and CoFe2O4 and their surface modification by surfactant adsorption. *Bull. Korean Chem. Soc*. **2006**, *27*, 237–242. https://doi.org/10.5012/bkcs.2006.27.2.237

Zheng, X.; Zheng, H.; Zhou, Y.; Sun, Y.; Zhao, R.; Liu, Y.; Zhang, S. Enhanced adsorption of Orange G from aqueous solutions by quaternary ammonium group-rich magnetic nanoparticles. *Colloids Surf. Physicochem. Eng. Asp*. **2019**, *580*, 123746. https://doi.org/10.1016/j.colsurfa.2019.123746